PERGAMON

Journal of Structural Geology 24 (2002) 1991–2005

JOURNAL OF STRUCTURAL GEOLOGY

www.elsevier.com/locate/jstrugeo

Cation ordering in omphacite and effect on deformation mechanism and lattice preferred orientation (LPO)

Frank E. Brenker[a,*], Dave J. Prior[b], Wolfgang Friedrich Müller[c]

[a]*Institut für Mineralogie und Geochemie, Universität zu Köln, Zülpicher Str. 49b, 50674 Köln, Germany*
[b]*Department of Earth Sciences, Liverpool University, Liverpool L69 7GP, UK*
[c]*Institut für Mineralogie, Technische Universität Darmstadt, Schnittspahnstr. 9, 64287 Darmstadt, Germany*

Received 8 May 2001; received in revised form 19 December 2001; accepted 9 January 2002

Abstract

We present microstructural data and lattice preferred orientations (LPOs) of omphacites from a suite of eclogites, from the Adula/Cima Lunga nappe (Central Alps). Our work shows a surprisingly strong correlation between the measured LPO and the ordering state of cations in omphacite. Estimates of deformation temperature from metamorphic petrology, together with measured omphacite compositions and LPOs, determine the field (ordering state), on the omphacite phase diagram, into which each sample falls. LPOs dominated by L-type and S-type signatures are developed in samples that fall in the P2/n field (ordered structure) and C2/c field (disordered structure), respectively.

Dislocations with $\mathbf{b} = 1/2\langle -110\rangle$ or $\mathbf{b} = [001]$ are observed in the transmission electron microscope (TEM) in all samples. The former change from a perfect dislocation in the C2/c structure to a partial in P2/n. Any movement of a partial dislocation requires the formation or growth of a stacking fault. Furthermore, in order to pass an obstacle a partial dislocation has to constrict to a unit dislocation. The energy to form a constriction is high in omphacite due to the large separation width. Thus, the activity of the $\mathbf{b} = 1/2\langle -110\rangle$ dislocation is hindered in the P2/n structure relative to the C2/c structure, which change the balance between the two and might give rise to the different LPOs.

Keywords: Electron backscatter diffraction (EBSD); Transmission electron microscope (TEM); Omphacite; Lattice preferred orientation (LPO); Order–disorder

1. Introduction

Models of subduction and exhumation of high-pressure and ultra high-pressure massifs critically depend on eclogite rheology. A basic assumption in the application of experimental rheological data is that there is no difference in deformation mechanisms in the experiment and in nature so that experimental flow-laws can be extrapolated across hundreds of degrees in temperature and across several orders of magnitude of strain rate. Thus, studies of naturally deformed rocks are an essential complement to laboratory experiments. Garnet rarely has a strong shape fabric in eclogites and most strain is accommodated by omphacite, which develops strong lattice preferred orientations (LPOs). Thus, understanding the mechanisms that lead to omphacite LPO is essential if we wish to apply experimental rheological data to geodynamic problems involving eclogites, e.g. the subduction and exhumation of oceanic crust.

To constrain better the mechanisms by which LPO of omphacite develops, and the parameters that control these, we have studied natural eclogites, with a range of deformation temperatures and compositions, from the Adula/Cima Lunga nappe (Central Alps; Fig. 1). A combination of electron backscatter diffraction (EBSD) and orientation contrast (OC) imaging in the scanning electron microscope (SEM), electron probe micro analysis (EPMA) and transmission electron microscopy (TEM) were used.

1.1. Omphacite LPOs

Helmstaedt et al. (1972) identified two principal types of LPOs in eclogites (Fig. 2). L-type LPO is characterised by a point maximum of [001] axes parallel to the lineation and [010] axes forming a girdle perpendicular to the lineation. S-type LPOs have the [001] axes and (010) planes parallel to the foliation. LPOs transitional between the L-type and S-type end-members are observed (Godard and Van Roermund, 1995). AF-type ('annealed fabric': Godard and Van Roermund, 1995) LPOs have [001] maxima parallel to the lineation and [010] maxima perpendicular to the lineation

* Corresponding author. Tel.: +49-221-470-6113; fax: +49-221-470-5199.
E-mail address: brenker@min.uni-koeln.de (F.E. Brenker).

0191-8141/02/$ - see front matter
PII: S0191-8141(02)00010-X

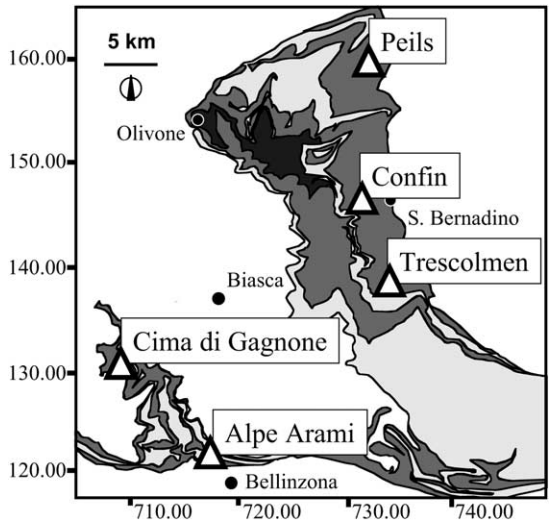

Fig. 1. Sketch map of the Adula/Cima Lunga nappe (Switzerland, Central Alps). Sample areas are indicated by rectangles.

but in the foliation. AF-type LPOs are associated with low temperature (450–550 °C) deformation. Random LPOs are typical of granoblastic eclogite xenoliths found in kimberlites (Helmstaedt et al., 1972).

1.2. Mechanisms of omphacite LPO development

1.2.1. Twinning

LPOs can be developed when deformation occurs by mechanical twinning, as is common in calcite (e.g. Burkhard, 1993). Limited deformation twinning, parallel to (100) or (001), is reported in omphacite (Van Roermund and Boland, 1981; Buatier et al., 1991; Philippot and Van Roermund, 1992; Godard and Van Roermund, 1995). Deformation twinning is common in shocked diopside from meteorites (Müller, 1993) but is rare in terrestrial samples. These data suggest that significant deformation twinning in clinopyroxene is only possible at low temperatures and very high strain rates.

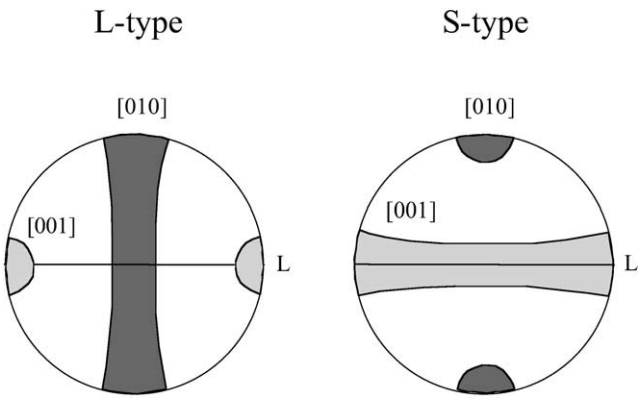

Fig. 2. Classification of pyroxene LPOs after Helmstaedt et al. (1972). (A) The L-type is characterised by [001] axes, which lie parallel to the lineation and (010) poles in a plane normal to the lineation. (B) S-type LPOs, in which the [001] axes lie in the foliation plane and (010) planes are parallel to the foliation.

1.2.2. Dislocation creep

Dislocation creep deformation generates LPOs (Paterson and Weiss, 1961; Wenk and Christie, 1991). A combination of dislocation creep and diffusive mass transfer is suggested as the most common creep mechanism in omphacite (e.g. Godard and Van Roermund, 1996). The most common glide systems (summarised by Godard and Van Roermund, 1995) are (100)[001], {110}[001] and {110}1/2⟨110⟩ (Van Roermund and Boland, 1981; Buatier et al., 1991; Philippot and Van Roermund, 1992; Godard and Van Roermund, 1995). At low temperatures (010)[100] was also identified (Philippot and Van Roermund, 1992). Dislocations with burgers vector 1/2⟨112⟩ were observed only in dislocation networks (Godard and Van Roermund, 1995).

Creep data are now available for eclogite (Jin et al., 2001) and include data for omphacite. However these new data do not describe omphacite microstructures, and do not characterise the omphacite slip systems so that experimental data for diopside are the most applicable in studying dislocation creep mechanisms in omphacite. In their experiments on single crystals of diopside Raterron et al. (1994) recognised a predominance of glide system {−110}1/2⟨110⟩ above 1000 °C. At intermediate temperatures (800 °C $< T <$ 1000 °C) (100)[001] slip systems dominate.

Van Roermund (1984) found a dominance of {hk0}[001] slip in natural omphacite samples deformed at 12 kb/500 °C.

1.2.3. Preferred growth

Godard and Van Roermund (1995) found a correlation between shape fabrics and LPOs of omphacite and discuss growth of omphacite in a preferred orientation as a mechanism for generating LPOs. Growth and dissolution rates are much faster in the [001] direction than in the [100] direction, which are in turn faster than in the [010] direction (Van Panhuys-Sigler and Hartman, 1981; Godard and Van Roermund, 1995). Syntectonic omphacite veins, where the [001] axes are perpendicular to the walls of the vein suggest that this growth rate anisotropy can lead to an LPO (Philippot and Van Roermund, 1992; Tsujimori, 1997). Mauler et al. (2001) suggest that anisotropic growth and dissolution can explain L- and S-type fabrics. Philippot and Van Roermund (1992) suggest that grain growth due to annealing is the mechanism that forms AF-type LPOs. S-type fabrics are observed in diopside aggregates produced by hot isostatic pressing prior to deformation experiments (Mauler et al., 2000a,b). These are interpreted as the result of rigid rotation of individual crystals which are elongated parallel to [001] and are shortest parallel to [010].

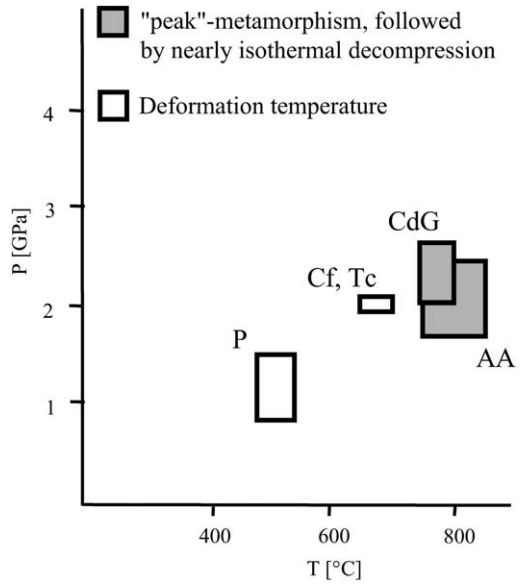

Fig. 3. Plot of estimated pressure and temperature conditions of the deformation for the samples studied in this work. P—Peils, Cf—Confin, Tc—Trescolmen, CdG—Cima di Gagnone, AA—Alpe Arami. For sample 163a28 (CdG) and AAX2B 8 (AA) these estimates record the peak PT conditions followed by rapid isothermal decompression. In some cases P96-4 (P), Cf96-4 (CdG), Tc 96-6 and Tc97-2 (Tc) a closer approximation of the deformation conditions was possible based on detailed PT data and their relation to phase petrology. Details and source references are given in the text.

2. Samples

The eclogites of the Adula/Cima Lunga nappe in the Central Alps are ideally suited to a study of omphacite LPO as a function of deformation conditions. The general increase in pressure and temperature from north to south, the high variability in chemical composition and the well documented geological history favours this nappe as a natural laboratory. Details of thermal and deformational history for each sample region are given below. The lithologies of the examined samples are quite similar. The eclogites are all dominated by the two minerals omphacite (40–60 vol%) and garnet (20–40 vol%). Minor amphibole, which is in part secondary, range between smaller than 5 vol% in sample AAX2B up to 20 vol% in sample P96-4. Only sample Cf96-4 shows a minor amount of primary quartz. Rutile and ilmenite occur as accessory minerals in all samples. Additional accessory phases are kyanite in sample AAX2B and white mica in sample P96-4.

2.1. Geological outline

The Adula/Cima Lunga nappe belongs to the Penninic nappe pile of the Central Alps (Switzerland). A detailed geotectonic model is compiled by Schmid et al. (1996). The Adula/Cima Lunga unit was part of the southernmost European plate.

Subduction of the unit starts at ca. 50 Ma with convergence rates of 1.2 cm/a (Dewey et al., 1989) to 1.5 cm/a (Schmid et al., 1996). The age of the peak metamorphism is estimated around 40 Ma (Becker, 1993; Gebauer, 1994). A further metamorphic episode during uplift is documented by U/Pb-chronometry at 33 Ma (Gebauer, 1994). The so called Lepontin-dome metamorphism took place after nappe stacking around 27 Ma (Vance and O'Nions, 1992). The main penetrative foliation in the country rocks was formed during nappe stacking. The structure of the eclogite boudins cannot be related to the regional kinematic framework as they are restricted to mafic and ultramafic high pressure boudins and predate all penetrative features of the country rocks. For further details see Brenker (1998) and references therein.

2.2. Deformation temperatures and pressures

The temperatures and pressures experienced by each sample are constrained from published phase petrology and major element exchange thermobarometry data. In the simplest cases, these estimates are likely to record the peak PT conditions that immediately preceded a rapid isothermal decompression. In some cases a closer approximation of the deformation conditions was possible based on detailed PT data and their relation to phase petrology. Fig. 3 summarises the PT estimates and the errors for each sample.

2.2.1. Peils (P96-4)

Based on element exchange equilibrium and mineral reactions Löw (1986) determined four phases of regional plastic deformation for the region of the northern Adula nappe. The eclogite facies metamorphism was reached at the beginning of D2. PT conditions of this deformation phase were determined as 470–540 °C and 1.2–1.5 GPa (peak metamorphic conditions). The subsequent fast exhumation of the unit up to 0.8 GPa took place around 500 °C. Any further deformation was restricted to rock types surrounding the eclogite boudins.

2.2.2. Confin (Cf96-4) and Trescolmen (Tc96-6, Tc97-2)

Meyre et al. (1997) determined a detailed quantitative pressure, temperature and deformation path of the middle Adula nappe using phase stability grids and element partitioning between garnet and clinopyroxene. Both sample regions, Trescolmen and Confin belong to this subunit. Four deformation phases D1–D4 can be distinguished. Texture forming took place during D1 (Trescolmen deformation phase; Meyre et al., 1997) and recrystallisation of the eclogite during early stages of decompression. Peak metamorphic conditions were determined to be 19–21 kb/650–700 °C (Meyre et al., 1997). The exhumation path shows an isothermal decompression, which restricts further deformation to conditions close to the maximum temperature.

Table 1
Representative electron microprobe analyses of omphacite compositions for samples described in this work

Sample	P96-4 o7	Cf96-4 o1	Tc96-6 o2	163a28 o1	AAX2B o1 p1
SiO_2	55.17	55.54	55.80	55.30	54.97
Al_2O_3	10.06	9.72	9.88	10.72	11.66
FeO	6.31	3.43	4.62	3.48	2.77
MgO	7.71	9.76	9.08	9.74	9.46
CaO	12.71	14.88	13.30	14.88	14.81
Na_2O	7.02	5.37	6.23	5.45	5.16
K_2O	0.00	0.01	0.00	0.00	0.00
TiO_2	0.04	0.05	0.09	0.14	0.17
P_2O_5	0.00	0.00	0.00	0.00	0.01
MnO	0.03	0.03	0.03	0.04	0.04
Cr_2O_3	0.00	0.02	0.05	0.04	0.05
NiO	0.01	0.02	0.02	0.03	0.02
Total	99.06	98.82	99.10	99.82	99.09

2.2.3. Cima di Gagnone (163a28)

A detailed PTD-path for the Cima di Gagnone area is given by Grond et al. (1995). Five deformation phases D0–D4 can be distinguished in different rock types in this area. D0 is only recognised in the mafic and ultramafic boudins. The omphacite texture in eclogites is produced under high pressure conditions during or close to the peak metamorphic event (Grond et al., 1995). A maximum temperature of 800 °C at 2–2.5 GPa is calculated by Grond et al. (1995) using Fe/Mg exchange reaction between garnet and clinopyroxene. The PT-path shows a slight cooling during the uplift of the high pressure rocks. Therefore a good estimate of the temperature during deformation is from 800 to 750 °C.

2.2.4. Alpe Arami (AAX2B)

For the Alpe Arami eclogites the thermal history is less well constrained and still a matter of debate (see Nimis and Trommsdorff, 2001a,b; Paquin and Altherr, 2001a,b). Most PT estimates are based on thermobarometric investigations of the garnet peridotite, which is surrounded by the eclogites studied in this work. Detailed PT-paths for the garnet peridotite are given by Brenker et al. (1997a,b), Paquin and Altherr (2001a,b), Nimis and Trommsdorff (2001a,b). Recent PT-calculations of Tappert (1999) yield 750 ± 30 °C, 2 ± 0.4 GPa for the eclogite. Our own measurements and calculations based on the Fe/Mg exchange reaction between garnet and clinopyroxene using calibrations of Krogh (1988) and Ellis and Green (1979) gave slightly higher peak temperatures of 800 ± 50 °C. An exhumation path determined by Paquin and Altherr (2001a), shows an isothermal exhumation, so that we can assume that the main deformation must have taken place close to the peak temperature.

The samples divide broadly into two high temperature samples (>750 °C: Cima di Gagnone and Alpe Arami) two medium temperature samples (650–700 °C: Confin and Trescolmen) and a low temperature sample (450–550 °C: Peils). All discussion of data will be made with reference to these temperature sub-divisions.

3. Methods

A polished thin section was prepared from each sample and carbon coated for EPMA. EPMA used wavelength dispersive detectors on a Jeol 8900 Superprobe with a 20 nA beam current and 20 kV accelerating voltage. Semi-quantitative element maps were also collected.

The carbon coating was removed after EPMA measurements and the thin section polished using a chemical-mechanical (SYTON) method (Fynn and Powell, 1979), so that EBSD and OC imaging could be conducted. OC imaging, using forescatter detectors (Prior et al., 1996) was used to identify domains of differing crystallographic orientation (c.f. Trimby et al., 1998). EBSD (Prior et al., 1999) was then used to measure the full crystallographic orientation of each domain identified. OC imaging and EBSD were conducted on a Philips XL30 scanning electron microscope, using 20 kV accelerating voltage and about 3 nA beam current. Channel + software was used to index EBSD patterns. Recent studies have applied automated EBSD in addition to manual EBSD (Mauler et al., 2000a, b, 2001; Bascou et al., 2001).

Disks of 3-mm-diameter were drilled out of the polished sections, using a 'Medenbach' microdrill attached to a microscope, and prepared for TEM. The epoxy was removed, using chloroform, the disks were mounted on copper grids and ion thinned to electron transparency. The thinned disks were coated with a very thin layer of carbon. A second thin section of each sample was prepared directly for TEM work (using crystal bond adhesive, which is removed using acetone). TEM work was performed using a Philips CM 12 with 120 kV acceleration voltage and an attached energy dispersive detector (EDAX 9900). Standard

Table 2
Calculated mean jadeite contents and variation of the studied samples

Sample	P96-4 o7	Cf96-4 o1	Tc96-6 o2	163a28 o1	AAX2B o1 p1
X_{Jd}	0.47	0.42	0.45	0.45	0.46
1 sigma	0.02	0.01	< 0.01	0.01	< 0.01
	VdL	VdSM	Cabo Ortegal		
X_{Jd}	0.38–0.54	0.41–0.58	0.3–0.37		

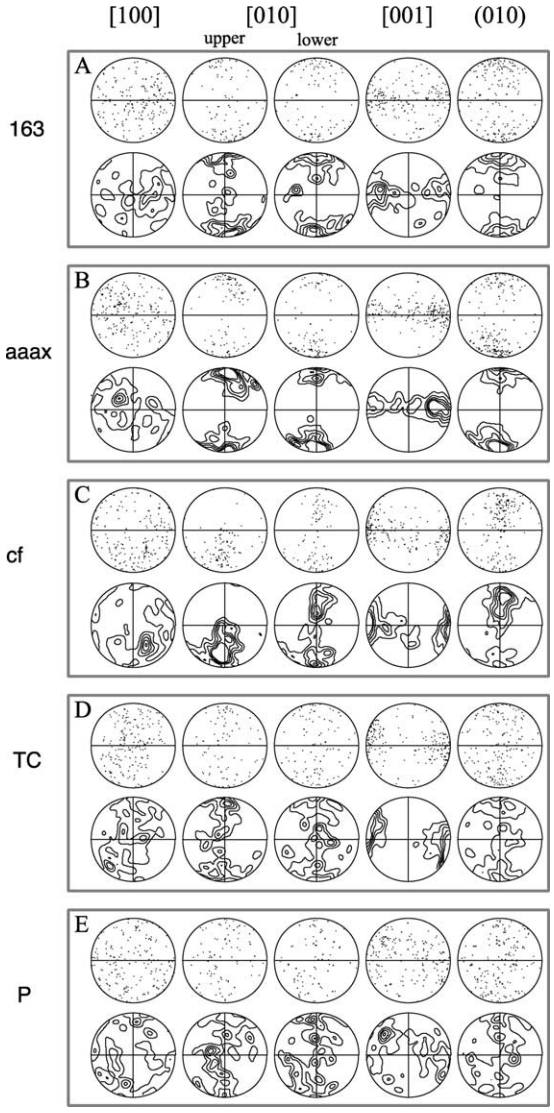

Fig. 4. Pole figures for EBSD data for the five samples examined in this study. (a) 163a28, (b) AAX2B, (c) Cf96-4, (d) Tc96-6, (e) P96-4. Each data set comprises 200 data points except (b), which comprises 218. Stereonets are equal area. [100], [001] and (010) are plotted in the lower hemisphere. [010] and [0 − 10] are distinguishable so that [010] are plotted on the entire sphere. Contouring used a counting circle on the sphere with a 40° opening angle. Contours are in multiples of uniform density. Foliation is marked by the horizontal line in each stereonet. Lineation is at the intersection of foliation and the primative.

techniques like 'weak beam' and selected area electron diffraction (SAED) were used. Antiphase boundaries were characterised using reflections of the type $h + k = \text{odd}$ (Phakey and Ghose, 1973). Burgers vectors of dislocations were identified using the $\mathbf{g}\cdot\mathbf{b} = 0$ invisibility criteria.

4. Results

4.1. Omphacite compositional range

The compositional range of each sample is very narrow (Tables 1 and 2). In all samples except AAX2B, the omphacite composition is inhomogeneous, due to a preserved growth zoning, which is only moderately overprinted by diffusion. Sample AAX2B reaches the highest peak-temperatures of all samples. It is likely that fast diffusion at high temperatures and probably the longer duration of the peak metamorphism and/or recrystallisation chemically homogenised this sample.

4.2. Omphacite LPO

4.2.1. High temperature (>750 °C)

In both 163a28 (Fig. 4a) and AAX2B (Fig. 4b) the [001] axes show a well-defined girdle parallel to the foliation. In AAX2B there is a single maximum, on the girdle, misoriented about 30° from the lineation. There are two, more diffuse, maxima on the girdle in 163a28. The poles to (010) planes in both 163a28 and AAX2B cluster close to the pole to foliation. AAX2B has a slightly stronger (010) fabric. In AAX2B clusters are slightly rotated clockwise from the poles to foliation. EBSD can distinguish the [010] and [0 − 10] axes, so that the whole sphere is needed to display [010] axes. In both samples, the [010] axis distribution in the lower hemisphere is very similar to that in the upper hemisphere, indicating that the [010] and [0 − 10] axis fabrics are equivalent. In both samples the [100] axis fabric is weak. Both LPOs are close to the S-type end member (Helmstaedt et al., 1972) end member (Fig. 2).

4.2.2. Medium temperature (ca. 650–700 °C)

The [001] axes in both Cf96-4 (Fig. 4c) and Tc96-6 (Fig. 4d) form well-defined point maxima close to the lineation. In both cases the [001] clusters are rotated slightly clockwise from the lineation. In both cases the poles to the (010) planes are distributed on a great circle, perpendicular to the lineation. In Tc96-6 there are no well-defined maxima within the (010) girdle and the [010] and [0 − 10] axes have equivalent fabrics. In Cf96-4 there is a strong maximum within the (010) girdle, oriented about 40° from the normal to foliation. Curiously, the upper and lower hemisphere plots of the [010] axes are quite different, indicating that the [010] and [0 − 10] axes do not have equivalent fabrics in Cf96-4. The [100] axes in Tc96-6 define a weak, although clear, great circle, sub-perpendicular to lineation. The [100] axes in Cf96-4 are less well-defined. The point maximum of [001] parallel to lineation is characteristic of L-type LPOs (Helmstaedt et al., 1972), although the distribution of [010] axes is transitional between L-type and S-type. Overall both LPOs are closer to the L-type end member (Fig. 2).

4.2.3. Low temperature (ca. 450–550 °C)

P96-4 has the weakest of the LPOs measured (Fig. 4e). The [001] axes are not strongly clustered. There is an absence of [001] axes in the direction normal to foliation. The poles to the (010) planes form a broad, weak girdle

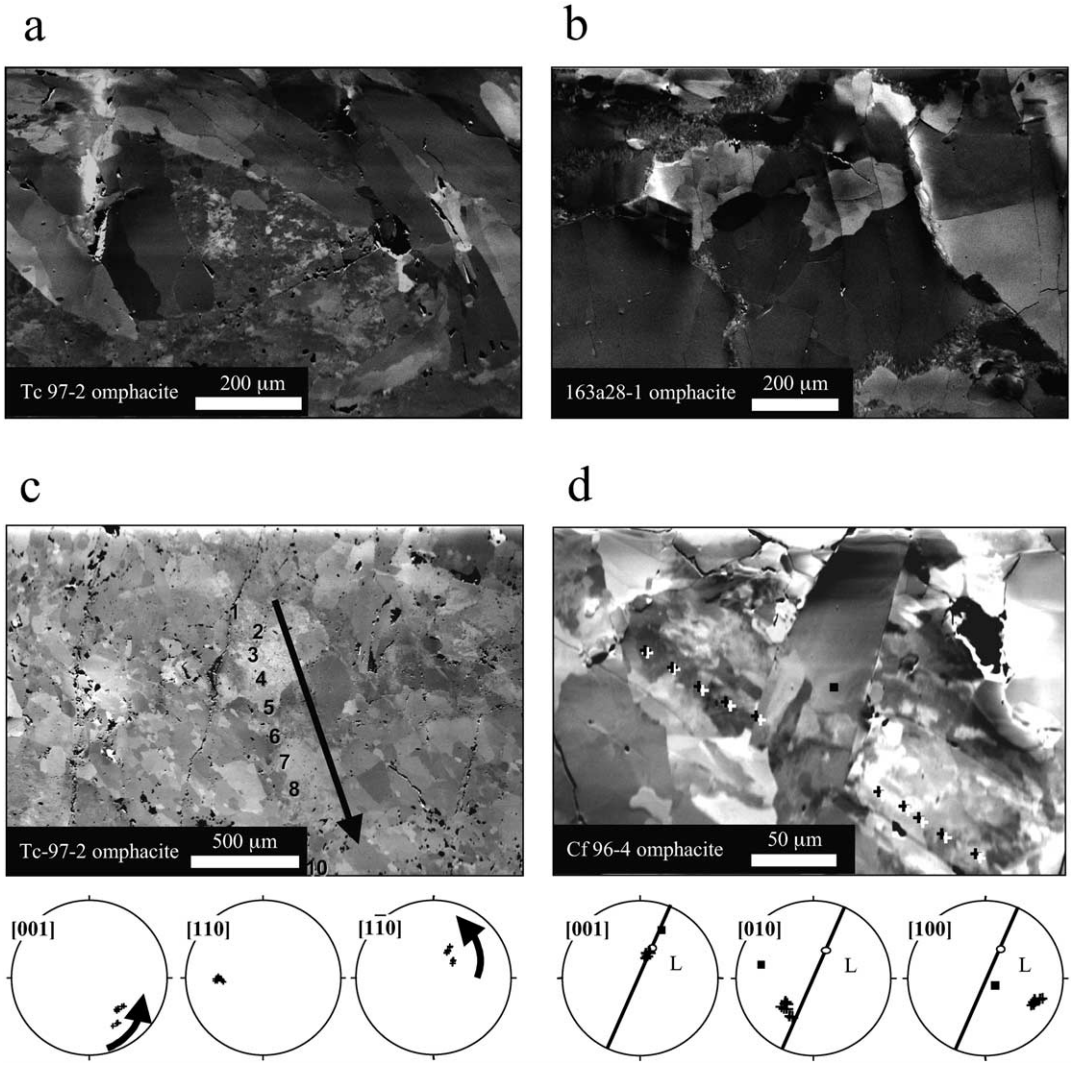

Fig. 5. (a) Orientation contrast image (OC) of sample 163a28-1 (Cima di Gagnone). The central part is occupied by a large omphacite crystal. Just a few subgrains >200 μm are visible. (b) Orientation contrast image (OC) of sample Tc97-2 (Trescolmen). Two generations of omphacite are visible. The first generation shows a cloudy distribution of orientations due to numerous small (<1 μm) subgrains. A second generation, overgrowing this microstructure, is characterised by grains with little internal structure. (c) OC image of the first generation of omphacite in sample Tc97-2 (Trescolmen). Individual measurement points for electron backscatter diffraction (EBSD) are indicated by numbers. Lower hemisphere, equal area projection of [001], [110] and [1 − 10] axes. (d) OC image of sample Cf96-4 (Confin) which where deformed at $T = 650–700$ °C. A second generation omphacite growth over an older subgrain rich area. EBSD measurement points are marked on the image. Lower hemisphere, equal area plot of EBSD measurements for [001], [010] and [100] axes of omphacite (– = foliation, dot = lineation). Crosses and rectangles indicate measurements from the subgrain-rich area and the second generation of omphacite, respectively.

perpendicular to lineation. Their upper and lower hemisphere [010] axis plots are similar, indicating that [010] and [0 − 10] fabrics are equivalent. The [100] axes are random. The (010) girdle places the LPO closest to the L-type end member although this is not as clear as the medium temperature samples.

4.3. Omphacite grain and subgrain-scale microstructure SEM

4.3.1. High temperature (>750 °C)

The general grain size in the high temperature samples is around 200–400 μm for the short axes and up 1 mm for the long axes. OC images show that most omphacite has no substructure. Large (>200 μm) subdomains, with sharp, straight to irregular boundaries are sometimes present (Fig. 5a). There are more diffuse boundaries within these subdomains that divide each into poorly defined 50–100 μm subdomains (Fig. 5a). EBSD measurements show that the misorientations across subdomain boundaries are mostly large (>10°, with no consistent misorientation axis.

The more diffuse boundaries are most likely to correspond to complex dislocation networks found in some rare cases using TEM.

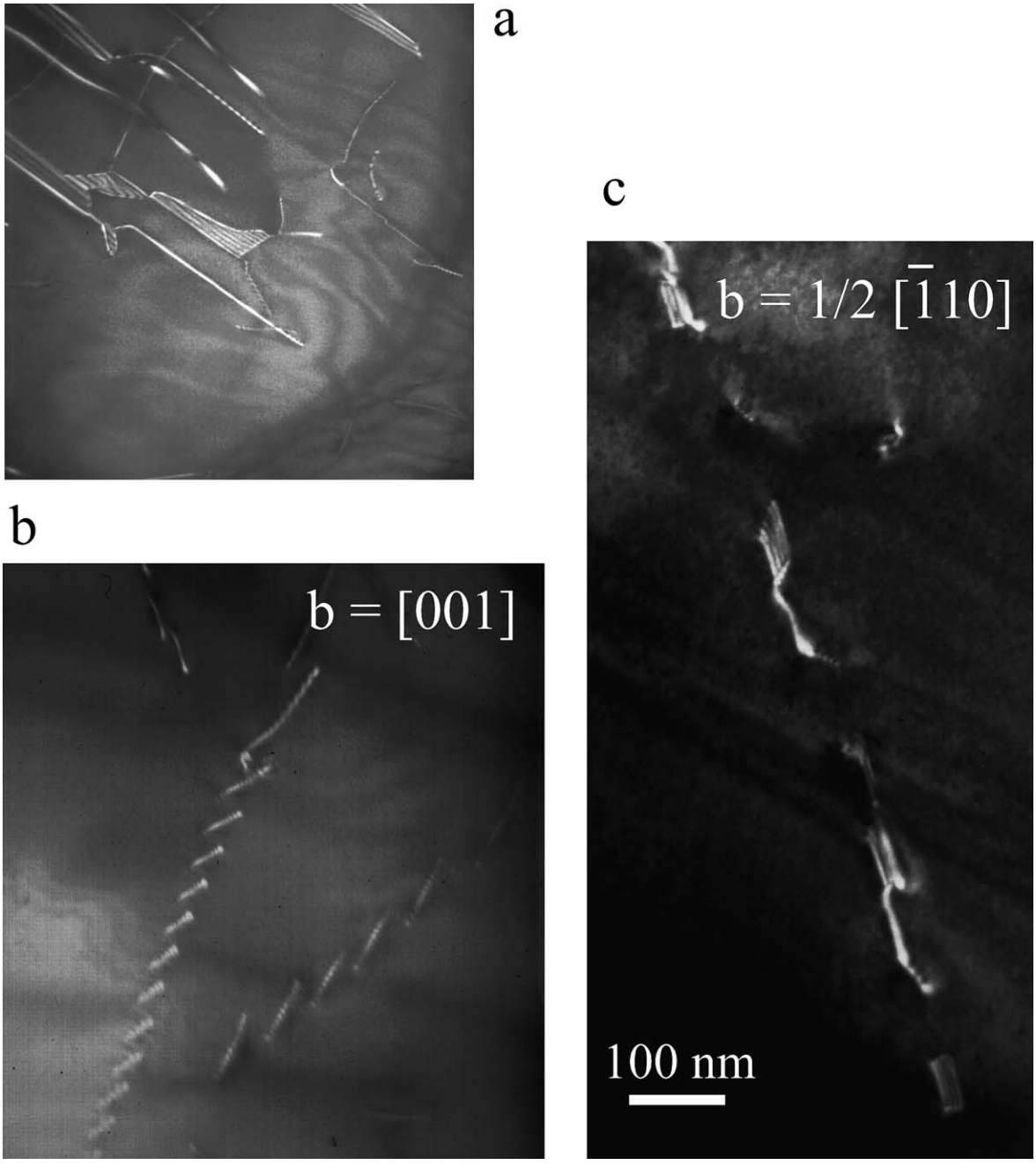

Fig. 6. (a) Weak beam TEM micrographs of a subgrain boundary in omphacite in sample AAX2B. A complex network of $\mathbf{b} = [001]$ and $\mathbf{b} = 1/2\langle -110\rangle$ dislocation can be seen. Subgrain boundaries are rare in this sample. (b,c) Weak beam TEM micrographs of sample Tc97-2 showing an arrangement of simple tilt walls consisting of (b) $\mathbf{b} = [001]$ and (c) $\mathbf{b} = 1/2[-110]$ dislocation, In (c) you can also see the stacking faults between dissociated $\mathbf{b} = 1/2[-110]$ dislocations.

4.3.2. Medium temperature (ca. 650–700 °C)

The samples show a bimodal grain size distribution due to recrystallisation. The larger grains are similar in size to the high temperature samples with up to 400 μm diameter. Additionally, smaller grains with 10–40 μm grain size occur. OC images show that the omphacite in these samples also contain two contrasting omphacite microstructures, which correspond to the grain size. The microstructure of 50–60 vol% of the grains are very similar to that in the high temperature samples, with very little substructure (Fig. 5b) but smaller grain size. In the remaining 40–50 vol%, the large grains are extensively subdomained. Although small (1–20 μm) subdomains dominate, some subdomains reach a few hundred micrometres (Fig. 5b). Insufficient neighbouring grain data (Wheeler et al., 2001) were collected to enable a statistical analysis of misorientation axes in an inverse pole figure. The misorientations across individual boundaries is too low for accurate calculation of

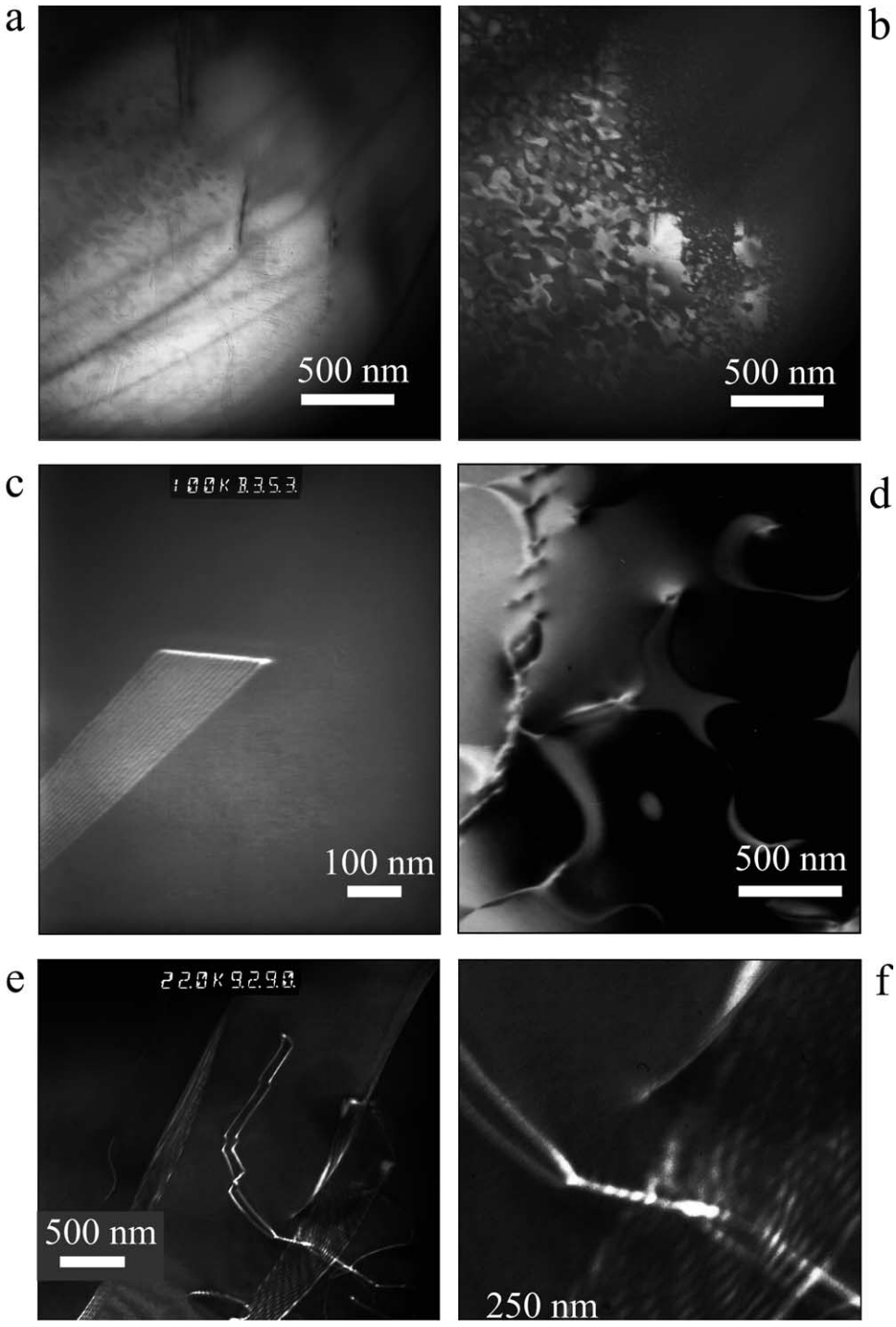

Fig. 7. TEM micrograph of sample AAX2B (Alpe Arami). (a) Bright field image showing the positions of dislocations with burgers vector $\mathbf{b} = 1/2[-110]$. (b) Dark field image of the same area. Dislocations are located at the border of two different sizes of APDs. The two APD sizes correspond to different compositional domains. Intense coarsening of APDs is restricted to a narrow region around the dislocations indicating limited movement after ordering of cations. (c) Dark field weak beam TEM micrograph of a partial dislocation in P2/n omphacite. The stacking fault, which is the product of movement of the partial dislocation, is in contrast. (d) Dark field TEM micrographs of samples from Trescolmen. Strong interaction between dislocations having burgers vector $\mathbf{b} = 1/2[1\ -\ 10]$ and APDs are shown. (e) Dark field 'weak beam' TEM micrograph showing the dissociation of dislocations, having burgers vector $\mathbf{b} = [-110]$, into two partials. (f) The blow up of TEM micrograph (e), shows a constriction of partial dislocations in order to cross an obstacle, in this case a subgrain boundary.

misorientation axes (Prior, 1999). Misorientation axes were calculated from the dispersions of data measured on transects (Boyle et al., 1998; Prior et al., 1999). EBSD measurements were made on transects across subdomain structures. Whilst the misorientations across any individual boundary are small, the data from the whole transect often show dispersions that indicate that misorientation axes correspond to a single crystallographic direction. In two transects in Cf96-4 one of the (110) poles or one of the [110] directions form a tight cluster, whilst other crystallographic orientations are distributed on trajectories that correspond to rotations around these (e.g. Fig. 5c). On another transect the [001] directions form a tight cluster (Fig. 5d) and all other directions are dispersed on small circle trajectories around this. In sample Tc97-2 one transect shows well-defined dispersions around (110) and another a less well-defined dispersion around (100). The large grain with few subdomains in Fig. 5d has a distinct orientation from the average orientation of the subdomained region. In this case the (010) is closer to the pole to foliation. We do not have sufficient data to generalise about the relative orientations of subdomained and un-subdomained grains.

4.3.3. Low temperature (ca. 450–550 °C)

The general grain size is around 10–40 μm determined using the optical microscope. Based on the weak preferred orientation this sample was not investigated in further detail using SEM or TEM techniques.

4.4. Omphacite dislocations, antiphase domains and their mutual interaction. TEM

4.4.1. High temperature (>750 °C)

TEM images show that free dislocation densities are very low ($<10^6$ cm^{-2}) in these samples. A few complex dislocation networks were found (Fig. 6a). Dislocations with $\mathbf{b} = 1/2\langle 110\rangle$ and $\mathbf{b} = [001]$ occur as free dislocations and were also identified in dislocation networks. Dislocations with $\mathbf{b} = 1/2\langle -110\rangle$ are dissociated. Dissociation widths are small and interaction with antiphase domain boundaries is moderate or absent. APDs are sometimes coarser around dislocations (Fig. 7a and b).

The mean size of APDs varies between 50 and 70 nm (Fig. 7b) and distinct sizes correspond to distinct compositional domains in the omphacite.

4.4.2. Medium temperature (ca. 650–700 °C)

TEM images of subdomain boundaries identified in OC images of strongly subdomained omphacite show that the boundaries comprise simple arrays of closely spaced dislocations (Fig. 6b and c). TEM analysis show that most subgrain walls are simple tilt walls formed by $\mathbf{b} = [001]$ dislocations (Fig. 6b). A few tilt walls with $\mathbf{b} = 1/2\langle -110\rangle$ dislocations were observed also (Fig. 6c). The $\mathbf{b} = 1/2\langle -110\rangle$ dislocations are always dissociated into two partials with a combined burgers vector of $1/2\langle -110\rangle$ (Fig. 7e) linked by a stacking fault (Fig. 7d). Dissociation widths of free dislocations can be very large and intense interaction with antiphase boundaries is always present (Fig. 7d).

Unbound dislocations, within subdomains, are rare. The unbound dislocations include $\mathbf{b} = 1/2\langle -110\rangle$ dislocations. APDs of up to 1000-nm-size are observed in strongly subdomained omphacite. There is extensive interaction between APDs and dislocations (Fig. 7d).

Omphacites that are not strongly subdomained have low ($<10^6$ m^{-2}) dislocation densities. Only a few dislocations were analysed having $\mathbf{b} = [001]$ burgers vector. Antiphase domain sizes in these omphacites are small (around 60 nm).

4.5. Deformation, recovery and recrystallisation mechanisms

The differences in microstructure, LPO and dislocation scale structure suggest a difference in the deformation mechanism between the high temperature samples and all other samples.

4.5.1. High temperature (>750 °C)

The presence of a strong LPO is suggestive of a dislocation creep deformation mechanism or stress sensitive oriented growth (Wenk and Christie, 1991). Based on observations of dislocations and subgrain walls we favour the first interpretation. Inheritance of the LPO from previous single crystal orientations (c.f. Jiang et al., 2000) is unlikely as the LPOs have the symmetry of the mesoscopic strain field. Generation of LPO by anisotropic growth and/or dissolution (Van Panhyus-Sigler and Hartman, 1981; Mauler et al., 2001) should give rise to L-type LPOs, rather than the observed S-types. The generally low dislocation density and restricted occurrence of subgrain structures suggests that dynamic recrystallisation processes are likely to have been fast, relative to dislocation generation and recovery, or that the microstructure has undergone significant thermal annealing. Although dynamic recrystallisation may influence LPOs (Knipe and Law, 1987), thermal annealing is shown to have little effect on LPO (Tullis, pers. comm., Ree and Park, 1997; Park et al., 2001) and it is likely that the LPO reflects the dislocation creep process.

4.5.2. Medium temperature (ca. 650–700 °C)

Subdomains juxtaposed by low angle boundaries that correspond to tilt walls are likely to be subgrains, suggesting a dislocation creep deformation mechanism accompanied by recovery. Coarser subgrain-free omphacite grains are likely to be the result of dynamic recrystallisation or annealing. There is insufficient data to assess the effect that this has on the LPO.

4.6. Origin and significance of antiphase domains

The ordering of cations due to the phase transition from C2/c omphacite to P2/n omphacite leads to the loss of a

translation symmetry element. Consequentely antiphase domain structures evolve. The antiphase vector is $\mathbf{R} = 1/2[-110]$. The mean size of antiphase domains in omphacite is a function of temperature and time. According to Carpenter (1981b) the antiphase domain coarsens with time at a given temperature by:

$$\delta^8 = 4.8 \times 10^{36} \exp(-75,000/\mathrm{R}T)t$$

where δ is the mean antiphase domain size, R the gas constant, T the temperature in Kelvin and t the time.

As the antiphase vector is the same as one of the two main burgers vectors, it is obvious that intense interaction between moving dislocations with $\boldsymbol{b} = 1/2[-110]$ and antiphase domain boundaries must occur in the P2/n structure. This process was documented by Van Roermund and Lardeux (1991) and Brenker (1998). Typically the interaction results in a rapid coarsening of antiphase domains. Such coarsening cannot be achieved by the normal time dependent coarsening process.

In most cases this results in a bimodal distribution (Van Roermund and Lardeux, 1991; Van Roermund, 1992; Brenker, 1998) of antiphase domain sizes. This effect can be used to distinguish deformation of omphacite in the ordered P2/n structure, where dislocations must interact with antiphase domains, from deformation in the C2/c structure, where no antiphase domain existed during dislocation activity.

Recrystallisation of omphacite resets the antiphase domain sizes to their original temperature dependent size and coarsening will start again from this point.

In all our medium temperature samples we found a strong interaction between dislocations and APDs. In the high-temperature samples no or only very limited interaction between APDs and dislocations were detected. APDs are significantly coarser in subdomained regions of medium-temperature samples than anywhere in high-temperature samples. These data suggest that the high-T samples deformed in the stability field of the C2/c disordered structure. All other samples deformed in the stability field of the P2/n ordered structure.

4.7. LPO, slip systems, and omphacite cation ordering state during deformation

4.7.1. Direct observations

$\mathbf{b} = [001]$ and $\mathbf{b} = 1/2\langle -110\rangle$ dislocations are observed in all samples in the TEM, suggesting that (100)[001], {110}[001] and {110}1/2⟨110⟩, the main slip systems of omphacite (Buatier et al., 1991; Van Roermund and Boland, 1981; Philippot and Van Roermund, 1992; Godard and Van Roermund, 1995) may be represented.

4.7.2. Misorientation axes

In the samples with L-type LPOs we can use the observed misorientation axes to constrain slip systems. Samples with S-type LPOs do not have sufficient misorientation axes and a similar analysis is not possible. For simple tilt walls the burgers vector is perpendicular to the misorientation axes and both of these are contained in the slip plane (Lloyd et al., 1997). The observed [001] and (110) misorientation axes can be explained by tilt walls comprising {110}[001]. Walls of only (110)[001] or (−110)[001] dislocations would give (110) misorientation axes. Equal numbers of (110)[001] and (110)[001] can build a twist wall that would give (100) misorientation axes. The observed misorientations can be explained by {110}[001] dislocations alone and it is these that are likely to be responsible for most strain in these samples. Other tilt or twist walls, including the {110}1/2⟨110⟩ and (100)[001] dislocations, give rise to misorientations that are not observed.

4.7.3. LPO data

If dislocation creep is the dominant mechanism, possible slip systems can be constrained, with caution, from the LPO data (Wenk and Christie, 1991). Bascou et al. (2002) have made a rigorous numerical model of LPO development in clinopyroxes. They have been able to generate S-type fabrics and fabrics similar to L-type, where [001] is clustered, but also with [010] clustered. Their numerical experiments show that both slip systems and strain-symmetry can affect the resulting LPOs. In our study, both TEM data and misorientation data suggest that slip systems are different in the high- and medium-temperature samples and we will explore, briefly and simplistically, how this might relate to observed LPOs. L-type LPOs could be explained by a dominance by $\mathbf{b} = [001]$, as the [001] axes cluster close to the lineation. Slip would need to occur on multiple planes to distribute the (010) evenly along the plane normal to lineation. The clustering of (010) axes 40° from the pole to foliation in sample Cf96-4 suggests that slip on multiple planes may not be possible and slip is dominated by the {110}[001]. The more even distribution of (010) normal to lineation in sample Tc96-6 may reflect greater significance of other slip systems in this sample. S-type LPOs do not infer a specific slip system as the [001] are distributed in the foliation. The (010) planes are sub-parallel to the foliation suggesting that these could be slip planes. The problem is that (010) is, as yet, not a recognised slip plane in omphacite. It is possible that the S-type LPOs may be explained by equal significance of {110}[001] and {110}1/2⟨110⟩ slip systems (Bascou et al., 2002).

4.7.4. Correlation of LPOs to the C2/c and P2/n omphacite structures

Our data show a strong correlation between the temperature of deformation and the resulting LPO. Godard and Van Roermund (1995), Abalos (1997) and Piepenbrier and Stöckhert (2001) also present LPO data for omphacite in samples where there are petrological constraints upon temperature and data for omphacite composition. A broad relationship between temperature and LPO was shown by Abalos (1997). The compositional

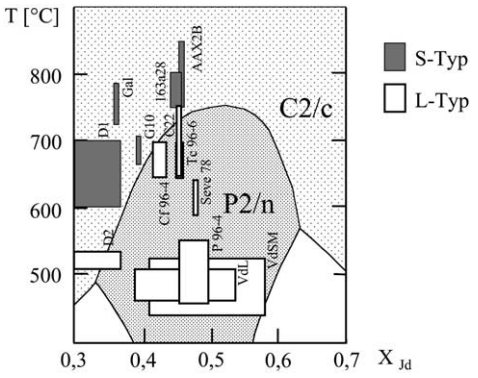

Fig. 8. Phase diagram of omphacite. The jadeite content of omphacite is plotted against the constrained deformation temperature. A strong correlation between LPO and ordering state during the deformation is obvious. Data from Abalos (1997, samples from deformation stage D1 and D2) and Godard and Van Roermund (1995, samples Gal, G10, C22 and Seve78) are added to the new data presented in this paper.

range of Cabo Ortegal samples was recalculated from the analysis given by Gil Ibarguchi et al. (1990). We have categorised their data as S- or L-type, calculated X_{Jd}-values and plotted these (Fig. 8) with our new data in the order–disorder phase diagram for omphacite (Carpenter, 1981a,b). A strong correlation between measured LPO and ordering state during deformation is apparent (Fig. 8). Furthermore all data of experimentally deformed clinopyroxene (e.g. Mauler et al., 2000a) reveal S-type LPO. The experiments were all conducted with C2/c pyroxenes and further strengthen our proposed correlation. This empirical analysis suggests that it is the order state of omphacite that controls the mechanisms by which omphacite deforms and through these, the LPOs generated. This idea will be tested as more omphacite LPO data is collected across a wider range of omphacite compositions and temperatures. Such data are now being collected rapidly. Bascou et al. (2001) and Mauler et al. (2001) both have extensive omphacite data sets although neither can be plotted on the omphacite order–disorder diagram because of lack of PT data (Mauler et al., 2001) or compositional data (Bascou et al., 2001).

The link of LPO to the order–disorder structure explains why some samples may not fit a simple relationship of LPO to temperature (Godard and Van Roermund, 1995) and why the L-type to S-type transition temperature characterised by Abalos (1997) is lower than that suggested by Brenker (1998). Only a suite of samples with constant omphacite composition will show a simple relationship of temperature and LPO.

4.7.5. Slip systems in the C2/c and P2/n omphacite structures

The $\mathbf{b} = 1/2\langle 110\rangle$ dislocation is a perfect dislocation in the C2/c space group (Fig. 9a). The ordering of cations in the P2/n structure leads to the doubling of the length of the burgers vector for a perfect dislocation to $\mathbf{b} = \langle -110\rangle$ (Fig. 9b). As the energy of a dislocation is proportional to the square of the length of the burgers vector, a splitting into two partials will be favoured due to a decrease of total energy by 50%. The dissociation mechanism is:

$$[-110] = \tfrac{1}{2}[-110] + \tfrac{1}{2}[-110]$$

or

$$[110] = \tfrac{1}{2}[110] + \tfrac{1}{2}[110].$$

Necessarily, a stacking fault exists between the dislocation pairs. Any further movement of a partial dislocation extends the stacking fault. Thus, the gain of interaction energy in the P2/n omphacite is counterbalanced by the stacking fault energy. Compared with the disordered C2/c omphacite the length of the burgers vector remains the same but an additional energy term due to the required stacking fault energy is added. For this reason $\mathbf{b} = 1/2\langle -110\rangle$ dislocations will be less mobile in the P2/n modification of omphacite than in the C2/c structure.

Furthermore the distance between the partials will be smaller if the stacking fault energy is higher. As known from studies of metals and alloys the movement of partial

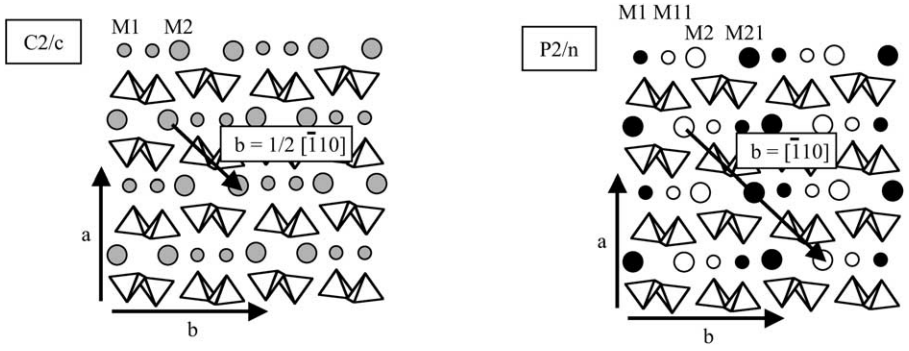

Fig. 9. Schematic sketch of the pyroxene structure viewed parallel to the *c*-direction. (a) C2/c pyroxene, an arrow indicates burgers vector $\mathbf{b} = 1/2[-110]$. The grey colour of M1 and M2 positions indicate disorder between Ca and Na on M2 and between Fe and Mg on M1. (b) P2/n pyroxene, black and white colours indicate ordering between Ca and Na on M2 and between Fe and Mg on M1. The ordering process leads to a doubling of the length of the burgers vector. This favours the dissociation of dislocations having burgers vector $\mathbf{b} = [-110]$ into two partials.

dislocations across a crystal is much more easily affected by obstacles than perfect dislocations, because the former are connected to a stacking fault. For example, extended screw dislocations cannot cross slip from one slip plane to another in order to pass an obstacle. This is possible, however, when the partials are constricted to a unit dislocation. The energy to form a constriction of partials depends on their separation and it is higher when the separation is large, i.e. when the stacking fault energy is low. It is well known that the dissociation width of dislocations has a significant effect on the work (strain) hardening of metals. Constrictions of split dislocations in omphacite can be seen in Fig. 7e and f where apparently the obstacle of a low angle grain boundary has to be crossed. The separation of partials was up to 60 nm. While it may seem an oversimplification to apply results obtained from face centred cubic metals directly to a mineral-like omphacite, there is hardly any doubt that the deformation behaviour of P2/n omphacite will be significantly different from that of C2/c. It can safely be concluded that the movement of partials of type $\mathbf{b} = 1/2\langle -110\rangle$ does demand more energy because stacking faults have to be formed and that these dislocations will be more easily pinned by obstacles in P2/n omphacite. Hence work (strain) hardening is much stronger and dynamic recovery due to cross slip and climb will become more difficult in C2/c omphacite. Slip systems having $\mathbf{b} = 1/2\langle -110\rangle$ dislocations will contribute less to the strain relative to $\mathbf{b} = [001]$ dislocations in P2/n omphacite.

Thus the balance of operating slip-systems must be different in the P2/n and C2/c structures and different LPOs may result from this alone, with no requirement to involve mechanisms other than dislocation creep.

We have already discussed data that suggest that the dominant slip systems were different in samples with S-type and L-type LPOs. An overall change in operating slip systems must also change the mechanical behaviour as discussed before and may promote more significant differences in deformation mechanisms operative in the two structures (in the significance of diffusion creep for example) or in the accompanying recovery and recrystallisation mechanisms. The microstructural evidence suggests that there are differences in the significance of recovery and recrystallisation in the high- and medium-temperature samples. These changes may be, in part, independent of a change of slip systems and may simply be a function of temperature. If this is the case, the microstructural changes across the P2/n to C2/c transition are likely to be different at different transition temperatures. Thus a comparison of omphacite microstructural changes across a low temperature transition ($X_{Jd} \sim 0.35$: e.g. Abalos et al., 1996) with the microstructural changes across a high temperature transition ($X_{Jd} \sim 0.5$: these samples), should help isolate any changes in recovery and recrystallization behaviour from changes in active slip systems.

4.7.6. Transitional fabrics between L- and S-types

All transitions between the two end member S-type and L-type can be recognised in nature. Even some of the samples presented in our work (e.g. 163a28) or in the work of Godard and Van Roermund (1995) do not belong to the pure end members described by Helmstaedt et al. (1972). This is not very surprising as other factors will affect LPO generation. An additional and important complication is that most PT paths for eclogites cross both stability fields and therefore allow deformation in both (ordered and disordered) structures. Indeed, all P2/n omphacites are thought to crystallise first with a C2/c structure, which subsequently starts to order. If deformation corresponds to the early stages of omphacite crystallisation, even if this is within the P2/n stability field, it will probably produce characteristics of the disordered C2/c structure.

4.7.7. Other factors in LPO development

It is clear that other parameters (Wenk and Christie, 1991) may influence LPO development. However, the strong correlation of LPO with the order–disorder diagram and the explanation of this in terms of dislocation activity suggest that the order– disorder state might be the prime control on LPO development in our samples and in those of Abalos (1997) and Godard and Van Roermund (1995). Godard and Van Roermund (1995) found a relationship between the shape and the LPO of omphacite. A change in shape fabric from oblate to prolate corresponds to the LPO transition from S-type to L-type. This has been strengthened by Mauler et al. (2001) who show a similar correlation. Mauler et al. (2001) explain L- and S-fabric types in terms of anisotropic growth and dissolution although modelling by Bascou et al. (2002) show that strain symmetry can control LPO in dislocation creep without requiring other mechanisms. Our view is that it is difficult to see how the strain could control LPO so that it corresponds to the order–disorder diagram. One way to explain the correlation observed by Godard and Van Roermund (1995) and Mauler et al. (2001) is that the deformation mechanisms and LPO control the strain and the shape fabrics, rather than vice versa.

It is tempting to pick examples of L-type high temperature LPOs as evidence against the model presented in this paper. However, one has to be careful. For example, Bascou et al. (2001) show an Alpe Arami sample with an L-type LPO: in contrast to the S-type LPO we measured. Beside the sample from Alpe Arami (AAX2B) studied in this work Brenker (1998) also found evidence for eclogite samples from the same area with omphacite compositions closer to $Di_{50}Jd_{50}$, which show strong interaction of dislocations and APDs suggesting deformation in the P2/n field. This correlation can be explained in two ways: either lowering the deformation temperature to 750 °C due to uncertainties in the thermobarometric calculation or increasing the transition temperature between P2/n to C2/c. Experimental data of Carpenter (1981a,b) suggest that the transition temperature

may be higher for Fe^{3+}, Mn-free samples (reaching 865 °C for $Di_{50}Jd_{50}$) than for the sample measured by Bascou et al. (2001) in the P2/n field for its composition (no compositional data are given).

We believe that order state will be a prime control on omphacite LPO. It will also be a function of many other parameters, including strain symmetry and deformation mechanisms other than dislocation creep. This highlights that studies of deformed omphacite need to collect the following data:

1. Outcrop scale structural information that might enable the strain symmetry to be constrained independently from the LPO. An unfortunate problem is that eclogites often comprise isolated blocks in lower grade rocks (as the samples in this study are) and the structural context is difficult to assess.
2. Omphacite compositional data.
3. Petrological and/or geochemical estimates of the PT of deformation. Again these are problematic; the critical problem being the distinction of peak PT from the PT of deformation.
4. Omphacite microstructures (EBSD and TEM) as a means of constraining deformation mechanisms.
5. Omphacite LPOs.

4.8. Implications

4.8.1. Omphacite LPO as a microstructural tool

If the relationship of LPO to the order–disorder phase diagram is correct, then omphacite LPO data together with the omphacite composition puts constraints on the deformation temperature, independently of any metamorphic PT data. If a range of omphacite compositions are available, omphacite LPO data may provide a precise microstructural thermometer: in eclogite facies layered gabbros, where different layers have different omphacite compositions for example. If the samples come from a sufficiently small area that deformation temperature can be assumed to have been the same in all samples then a change in LPO should occur at the omphacite composition corresponding to the change from the ordered to the disordered structure for that temperature.

4.8.2. Use of laboratory mechanical data for pyroxenes

Mechanical data for pyroxenes relate almost exclusively to diopside compositions. If P2/n omphacite behaves differently to C2/c omphacite then we cannot make a general, single extrapolation of diopside data to be representative of omphacite. We know, for example, that the thermal expansion of each differ (Pavese et al., 2000). A naive view might suggest that diopside, which has space group C2/c, data may be applicable to C2/c omphacite but not to P2/n omphacite. Understanding the rheology of eclogites requires good experimental data for omphacite, rather than for diopside or jadeite. Experiments that address the mechanical behaviour of both the P2/n and C2/c structures will be important.

4.8.3. Omphacite and eclogite rheology

The mechanical properties of P2/n and C2/c omphacite may be different. Intuitively a P2/n omphacite, with fewer slip systems, will be stronger than a C2/c omphacite at the same temperature, although the precise relationships will depend on how changes in slip systems affect other deformation mechanisms and the role of recrystallisation and this intuition may be proven wrong by experimental data. Whatever the details, the model presented here predicts that the rheology of eclogites is likely to change markedly at critical, temperature-dependent, omphacite compositions. Layered oceanic crust in the eclogite facies in a subduction zone may be rheologically stratified as a function of primary compositional layering.

4.8.4. Implications for seismic anisotropy

Different LPOs will give rise to different seismic anisotropies (e.g Mainprice and Humbert, 1994; Tommasi et al., 2000; Bascou et al., 2001). Thus the seismic anisotropy of eclogites will be influenced by both temperature and composition. Seismic data from subduction zones, together with a knowledge of the compositional stratification of the oceanic crust may enable mapping of subduction zone temperature fields.

5. Conclusions

The ordering of cations in omphacite may be a prime control on LPO formation and rheology. L-type LPOs are developed in samples that fall in the P2/n field (ordered structure), whereas S-type LPOs correlates with the C2/c field (disordered structure). The strong correlation between ordering state and LPO is further constrained by detailed TEM work.

The observed correlation is due to a change of $\mathbf{b} = 1/2\langle -110\rangle$ dislocations from perfect to partial dislocations depending on the ordering state of cations. The movement of partial dislocations is hindered due to the requirement to form a stacking fault and more dramatically because partial dislocation cannot cross slip or climb without constriction to a perfect dislocation. The energy to form a constriction is high in omphacite due to the large separation width. Thus, the activity of the $\mathbf{b} = 1/2\langle -110\rangle$ dislocation is hindered in the P2/n structure relative to the C2/c structure. Irrespective of any other differences, the different balance of slip-system activity in the P2/n and C2/c structures could give rise to different LPOs. The observed S-type and L-type LPOs are broadly compatible with dominance of the $\mathbf{b} = 1/2\langle -110\rangle$ and $\mathbf{b} = [001]$ dislocations, respectively.

The LPOs will further influence eclogite rheology and physical property anisotropies, such as seismic anisotropy.

Acknowledgements

We like to thank the DFG and NERC for support of this work. Furthermore we thank J. Kolb, Darmstadt for the preparation of the thin slices. The comments of S.A.T. Redfern and H. Van Roermund are gratefully acknowledged.

References

Abalos, B., 1997. Omphacite fabric variation in the Cabo Ortegal eclogite (NW spain) relationships with strain symmetry during high-pressure deformation. Journal of Structural Geology 10, 621–637.

Abalos, B., Azcarraga, J., Gil Ibarguchi, J.I., Mendia, S., Santos Zalduegui, J.F., 1996. Flow stress, strain rate and effective viscosity evaluation in a high-pressure metamorphic nappe (Cabo Ortegal, Spain). Journal of Metamorphic Geology 14, 227–248.

Bascou, J., Barroul, G., Vauchez, A., Mainprice, D., Egydiuo-Silva, M., 2001. EBSD measured lattice-preferred orientations and seismic properties of eclogites. Tectonophysics 342, 61–80.

Bascou, J., Tommasi, A., Mainprice, D., 2002. Plastic deformation and development of clinopyroxene lattice preferred orientations in eclogites. Journal of Structural Geology in press.

Becker, H., 1993. Garnet peridotite and eclogite Sm–Nd mineral ages from the Lepontine dome (Swiss Alps): new evidence for Eocene high-pressure metamorphism in the Central Alps. Geology 21, 599–602.

Boyle, A.P., Prior, D.J., Banham, M.H., Timms, N.E., 1998. Plastic deformation of metamorphic pyrite: new evidence from electron backscatter diffraction and forescatter orientation contrast imaging. Mineralium Deposita 34, 71–81.

Brenker, F.E., 1998. Mikrogefügethermochronometrie für Eklogite. Diss. J.W. Goethe-Universität, Frankfurt, Tectum-Verlag. 189pp.

Brenker, F.E., Müller, W.F., Brey, G.P., 1997. Mikrogefügethermo(baro)metrie (TEM) für Eklogite. European Journal of Mineralogy, Bh. Vol. 9-1.

Brenker, F.E., Müller, W.F., Brey, G.P., 1997b. Microstructure thermo(-baro)metry (TEM) for eclogites. Terra Nova, Supplement 1 (9), 4.

Buatier, M., Van Roermund, H.L.M., Drury, M.R., Lardeaux, J.M., 1991. Deformation and recrystallization mechanisms in naturally deformed omphacites from the Sesia–Lanzo zone: geophysical consequences. Tectonophysics 195, 11–27.

Burkhard, M., 1993. Calcite-twins, their geometry, appearance and significance as stress-strain markers and indicators of tectonic regime: a review. Journal of Structural Geology 15, 351–368.

Carpenter, M.A., 1981a. Omphacite microstructures as time–temperature indicators of blueschist- and eclogite-facies metamorphism. Contributions to Mineralogy and Petrology 78, 441–451.

Carpenter, M.A., 1981b. Time–temperature transformation (TTT) analysis of cation disordering in omphacite. Contributions to Mineralogy and Petrology 78, 433–440.

Dewey, J.F., Helmann, M.L., Turco, E., Hutton, D.H.W., Knott, S.D., 1989. In: Coward, M.P. (Ed.), Kinematics of the Western Mediteranean, in Alpinbe Tectonics, Geol. Soc. London Spec. Publ. 45, pp. 265–284.

Ellis, D.J., Green, D.H., 1979. An experimental study of the effect of Ca upon garnet–clinopyroxene Fe–Mg exchange equilibria. Contributions to Mineralogy and Petrology 71, 13–22.

Fynn, G.W., Powell, W.J.A., 1979. The Cutting and Polishing of Electro-optic Materials. Adams Hilger, London 216pp.

Gebauer, D., 1994. A P–T–t path for some high-pressure ultramafic/mafic rock-associations and their felsic country-rocks based on U–Pb SHRIMP-dating of magmatic and metamorphic zircon domains. Example: Swiss Central Alps. Abstract Volume. 16th General Meeting of the International Mineralogical Association. Societa Italiana di mineralogia e petrologia, Pisa, pp. 139–140.

Gil Ibarguchi, J.I., Mendia, M., Girardeau, J., Peucat, J.J., 1990. Petrology of eclogites and clinopyroxene–garnet metabasites from the Cabo Ortegal complex (northwestern Spain). Lithos 25, 133–162.

Godard, G., Van Roermund, H.L.M., 1995. Deformation-induced clinopyroxene fabrics from eclogites. Journal of Structural Geology 17, 1425–1443.

Godard, G., Van Roermund, H.L.M., 1996. Clinopyroxene deformation mechanisms in eclogites: dislocation creep or mass transfer? In: Treloar, P.T., O'Brien, P. (Eds.). What Drives Metamorphism and Metamorphic Reactions: Heat Production, Heat Transfer, Deformation and Kinetics? Kingston University, pp. 26–27.

Grond, R., Wahl, F., Pfiffner, M., 1995. Mehrphasige alpine Deformation und Metamorphose in der nördlichen Cima–Lunga-Einheit, Zentralalpen (Schweiz). Schweizer Mineralogisch Petrographische Mitteilungen 75, 371–386.

Helmstaedt, H., Anderson, O.L., Gavasci, A.T., 1972. Petrofabric studies of eclogite, spinel–websterite and spinel–lherzolite xenolths from kimberlite-bearing breccia pipes in southeastern utah and northeastern arizona. Journal of Geophysical Research 77, 4350–4365.

Jiang, Z., Prior, D.J., Wheeler, J., 2000. Albite CPO, grain misorientation distribution and granular flow in a low-grade mylonite. Journal of Structural Geology 22, 1663–1674.

Jin, Z.-M., Zhang, J., Green, H.W., II, Jin, S., 2001. Eclogite rheology: implications for subducted lithosphere. Geology 29, 667–670.

Knipe, R.J., Law, R.D., 1987. The influence of crystallographic orientation and grain boundary migration on microstructural and textural evolution in an *S–C* mylonite. Tectonophysics 135, 155–169.

Krogh, E.J., 1988. The garnet–clinopyroxene Fe–Mg geothermometer—a reinterpretation of existing experimental data. Contributions to Mineralogy and Petrology 99, 44–48.

Lloyd, G.E., Farmer, A.B., Mainprice, D., 1997. Misorientation analysis and the formation and orientation of subgrain and grain boundaries. Tectonophysics 279, 55–78.

Löw, S., 1986. Ein tektono-metamorphes Entwicklungsmodell der nördlichen Adula Decke. Schweizer Mineralogisch Petrographische Mitteilungen 66, 129–134.

Mainprice, D., Humbert, M., 1994. Methods of calculating petrophysical properties from lattice preferred orientation data. Surv. Geophys. 15, 575–592.

Mauler, A., Bystricky, M., Kunze, K., Mackwell, S., 2000a. Microstructures and lattice preferred orientations in experimentally deformed clinopyroxene. Journal of structural Geology 22, 1633–1648.

Mauler, A., Burlini, L., Kunze, K., Philippot, P., Burg, J.P., 2000b. P-wave anisotropy in eclogites and relationship to the omphacite crystallographic fabric. Phys Chem Earth Pt A 25 (2), 119–126.

Mauler, A., Godard, G., Kunze, K., 2001. Crystallographic fabrics of omphacite, rutile and quartz in Vendée eclogites (Armorican Massif, France). Consequences for deformation mechanisms and regimes. Tectonophysics 342, 81–112.

Meyre, C., de Capitani, C., Partzsch, J.H., 1997. A ternary solid solution model for omphacite and ist application to geothermobarometry of eclogites from the Middle Adula nappe (Central Alps, Switzerland). Journal of Metamorphic Geology 15, 687–700.

Müller, W.F., 1993. Thermal and deformation history of the Shergotty meteorite deduced from clinopyroxene microstructures. Geochimica et Cosmochimica Acta 75, 4311–4322.

Nimis, P., Trommsdorff, V., 2001a. Comment on "New constraints on the P–T evolution of the Alpe Arami garnet peridotite body (Central Alps, Switzerland)" by Paquin and Altherr. Journal of Petrology 42, 1773–1779.

Nimis, P., Trommsdorff, V., 2001b. Revised thermobarometry of Alpe Arami and other garnet peridotites from the Central Alps. Journal of Petrology 42, 103–115.

Paquin, J., Altherr, R., 2001a. New constraints on the P–T evolution of the Alpe Arami garnet peridotite body (Central Alps, Switzerland). Journal of Petrology 42, 1119–1140.

Paquin, J., Altherr, R., 2001b. "New constraints on the P–T evolution of the Alpe Arami garnet peridotite body (Central Alps, Switzerland)": reply

to comment by Nimis and Trommsdorff (2001). Journal of Petrology 42, 1781–1787.

Park, Y., Ree, J.H., Kim, S., 2001. Lattice preferred orientation in deformed-then-annealed material: observations from experimental and natural polycrystalline aggregates. International Journal of Earth Sciences 90, 127–135.

Paterson, M.S., Weiss, L.E., 1961. Symmetry concepts in the structural analysis of deformed rocks. Bulletin of the Geological Society of America 72, 841–882.

Pavese, A., Bocchio, R., Ivaldi, G., 2000. In situ high temperature single crystal X-ray diffraction study of a natural omphacite. Mineralogical Magazine 64, 983–993.

Phakey, P.P., Ghose, S., 1973. Direct observations of anti-phase domain structure in omphacite. Contributions to Mineralogy and Petrology 39, 239–245.

Philippot, P., Van Roermund, H.L.M., 1992. Deformation processes in eclogitic rocks: evidence for the rheological delamination of the oceanic crust in deeper levels of subduction zones. Journal of Structural Geology 14, 1059–1077.

Piepenbrier, D., Stöckhert, B., 2001. Plastic flow of omphacite in eclogites at temperatures below 500 °C—implications for interplate coupling in subduction zones. International Journal of Earth Sciences 90, 197–210.

Prior, D.J., 1999. Problems in determining misorientation axes, for small angular misorientations, using electron backscatter diffraction in the SEM. Journal of Microscopy 195, 217–225.

Prior, D.J., Trimby, P.W., Weber, U.D., Dingley, D.J., 1996. Orientation contrast imaging of microstructures in rocks using forescatter detectors in the scanning electron microscope. Mineralogical Magazine 60, 859–869.

Prior, D.J., Boyle, A.P., Brenker, F., Cheadle, M.C., Day, A., Lopez, G., Peruzzo, L., Potts, G.J., Reddy, S.M., Spiess, R., Trimby, P.W., Wheeler, J., Zetterström, L., 1999. The application of electron backscatter diffraction and orientation contrast imaging in the SEM to textural problems in rocks. American Mineralogist 84, 1741–1759.

Raterron, P., Doukhan, N., Jaoul, O., Doukhan, J.C., 1994. High temperature deformation of diopside IV: predominance of {110} glide above 1000 °C. Physics of the Earth and Planetary Interiors 82, 209–222.

Ree, J.H., Park, Y., 1997. Static recovery and recrystallization microstructures in sheared octachloropropane. Journal of Structural Geology. 19, 1521–1526.

Schmid, S.M., Pfiffner, O.A., Schreurs, G., 1996. Rifting and collision in the Penninic zone of eastern Switzerland. Geologic Structure and Evolution of the Alps 14, 160–185.

Tappert, R., 1999. Rekonstruktion des P,T,t-Pfades von Eklogiten der Cima–Lunga Einheit, Zentralalpen, Schweiz. Diplom thesis, J.W. Goethe-University, Frankfurt.

Tommasi, A., Mainprice, D., Canova, G., Chastel, Y., 2000. Viscoplastic self-consistent and equilibrium-based modeling of olivine lattice preferred orientations: Implications for the upper mantle seismic anisotropy. Journal of Geophysical Research—Solid Earth 105, 7893–7908.

Trimby, P.W., Prior, D.J., Wheeler, J., 1998. Grain boundary hierarchy development in a quartz mylonite. Journal of Structural Geology 20 (7), 917–935.

Tsujimori, T., 1997. Omphacite–diopside vein in an omphacitite block from the osayama serpentinite melange, Sangun–Renge metamorphic belt, southwestern Japan. Mineralogical Magazine 61, 845–852.

Vance, D., O'Nions, R.K., 1992. Prograde and retrograde thermal histories from the central Swiss Alps. Earth and Planetary Science Letters 114, 113–129.

Van Panhuys-Sigler, M., Hartman, P., 1981. Morphologie théoretique de certains pyroxénes deduite de la structure cristalline. Bulletin Minéralogy 104, 95–106.

Van Roermund, H.L.M., 1984. Omphacite microstructures from a spanish eclogite. Textures and Microstructures 6, 105–116.

Van Roermund, H.L.M., Boland, J.N., 1981. The dislocation substructures of naturally deformed omphacites. In: Lister, G.S., Behr, H.-J., Weber, K., Zwart, H.J. (Eds.), The Effect of Deformation on Rocks, Tectonophysics 78, pp. 403–418.

Van Roermund, H.L.M., Lardeux, J.M., 1991. Modification of antiphase domain sizes in omphacite by dislocation glide and creep mechanisms and ist petrological consequences. Mineralogical Magazine 55, 397–407.

Wenk, H.-R., Christie, J.M., 1991. Comments on the interpretation of deformation textures in rocks. Journal of Structural Geology 13, 1091–1110.

Wheeler, J., Prior, D.J., Jiang, Z., Spiess, R., Trimby, P.W., 2001. The petrological significance of misorientations between grains. Contributions to Mineralogy and Petrology 141, 109–124.